

Supporting Information

Rational Design of Chloride Ion Transport Channels in Open Borate Framework

Yu Meng,^{a,b} Naoyoshi Nunotani,^c Kazuki Shitara,^{*d} Yoshitaka Matsushita,^e Nobuhito Imanaka,^c

Kazunari Yamaura^{a,b} and Yoshihiro Tsujimoto^{*a,b}

^aResearch Center for Materials Nanoarchitectonics (MANA), National Institute for Materials Science, 1-1 Namiki, Tsukuba, Ibaraki 305-0044, Japan.

^bGraduate School of Chemical Sciences and Engineering, Hokkaido University, North 13 West 8, Kitaku, Sapporo 060-0808, Japan.

^cDepartment of Applied Chemistry, Faculty of Engineering, Osaka University, 2-1 Yamadaoka, Suita, Osaka 565-0871, Japan

^dNanostructures Research Laboratory, Japan Fine Ceramics Center, 2-4-1 Mutsuno, Nagoya, Aichi 456-8587, Japan

^eSurface and Bulk Analysis Unit, National Institute for Materials Science, 1-2-1 Sengen, Tsukuba, 305-0047, Japan

Table of Contents

	Title
Section S1	Experimental Procedures.
Figure S1	Stability of $\text{Ca}_2\text{B}_5\text{O}_9\text{Cl}$ in air, O_2 , and N_2 gas atmospheres.
Figure S2	Photographs of single crystals of undoped and La-doped $\text{Ca}_2\text{B}_5\text{O}_9\text{Cl}$.
Figure S3	EDX analysis of undoped and La-doped $\text{Ca}_2\text{B}_5\text{O}_9\text{Cl}$.
Figure S4	Density of states and band diagrams of $\text{Ca}_2\text{B}_5\text{O}_9\text{Cl}$.
Figure S5	Complex impedance plots of $(\text{Ca}_{1-x}\text{La}_x)_2\text{B}_5\text{O}_9\text{Cl}_{1+2x}$ ($x = 0, 0.05, 0.10$) recorded in an Ar gas atmosphere at 400, 500, and 700°C.
Figure S6	Comparison of the ac conductivity of $(\text{Ca}_{1-x}\text{La}_x)_2\text{B}_5\text{O}_9\text{Cl}_{1+2x}$ ($x = 0, 0.05, 0.10$) with those of conventional chloride-ion conductors.
Figure S7	TG-DTA curves of $x = 0.10$ in a N_2 gas atmosphere and room-temperature PXRD patterns before and after the TG-DTA measurements.
Figure S8	Polarization behavior for $(\text{Ca}_{1-x}\text{La}_x)_2\text{B}_5\text{O}_9\text{Cl}_{1+2x}$ ($x = 0.10$) in Ar gas atmosphere at 700°C.
Figure S9	Root square displacements for each Cl during MD simulations of the model containing a complex defect of La_{Ca} and Cl_i .
Figure S10	Root mean square displacements for the O _i model during MD simulations.
Table S1	Results of single-crystal structure analysis of undoped and La-doped $\text{Ca}_2\text{B}_5\text{O}_9\text{Cl}$.
Table S2	Structural parameters for the single crystal of $\text{Ca}_2\text{B}_5\text{O}_9\text{Cl}$.
Table S3	Anisotropic displacement parameters of $\text{Ca}_2\text{B}_5\text{O}_9\text{Cl}$.
Table S4	Structural parameters for the single crystal of La-doped $\text{Ca}_2\text{B}_5\text{O}_9\text{Cl}$.
Table S5	Anisotropic displacement parameters of La-doped $\text{Ca}_2\text{B}_5\text{O}_9\text{Cl}$.

Section S1. Experimental Procedures

Reagents. B₂O₃ (Sigma-Aldrich, 99.98%), CaCl₂ (Wako Pure Chemical Industries, 95.0%) powders were used as received. La₂O₃ (Rare Metallic, 99.99%) was heated overnight in a dry oven at 1000°C prior use. CaO was obtained by heating CaCO₃ (Rare Metallic, 99.99%) overnight in air at 950°C. All raw materials were stored in an Ar-filled glovebox (moisture and oxygen levels less than 0.1 ppm).

Crystal Growth. Single crystals of Ca₂B₅O₉Cl and (Ca_{0.92}La_{0.08})₂B₅O₉Cl_{1.16} were obtained by the flux growth method using a CaCl₂ molten salt. 4.5 mmol of B₂O₃, 2.7 mmol of CaO, and 1g of CaCl₂ for the undoped sample and 4.5 mmol of B₂O₃, 2.16 mmol of CaO, 0.18 mmol of La₂O₃, and 1g CaCl₂ for the La-doped sample were thoroughly mixed, loaded into a silica tube with a diameter of 11 mm, and flame-sealed under a vacuum level of 1 Pa. The starting materials were heated in a muffle furnace to 1000°C within 6h and held for 24h, cooled to 600°C at 5°C/h, and finally naturally cooled to room temperature by turning off the heater. The products were then washed with sonicated water and extracted from the flux. Colorless transparent rod-shaped crystals of Ca₂B₅O₉Cl and (Ca_{0.92}La_{0.08})₂B₅O₉Cl_{1.16} were collected by vacuum filtration, respectively.

Solid State Reaction. Polycrystalline powder samples of (Ca_{1-x}La_x)₂B₅O₉Cl_{1+2x} ($x = 0, 0.05, 0.10, 0.125, 0.15$) were synthesized from a stoichiometric mixture of B₂O₃, CaO, CaCl₂, and La₂O₃. The mixture was ground thoroughly with an agate mortar and pestle, pressed into a pellet with a diameter of 6.9 mm, flame-sealed under a vacuum level of 1 Pa, and then heated in a muffle furnace at 880°C for 24h and cooled to room temperature for 6h.

Elemental Analysis. Elemental analysis on the single crystals of undoped and La-doped Ca₂B₅O₉Cl was carried out using a scanning electron microscope (SEM, HITACHI-TM3000) equipped with an energy dispersive X-ray (EDX) spectrometer (Oxford Instruments, Swift ED3000). The accelerating voltage was 15 keV.

Single-Crystal Structure Determination. Single crystal X-ray diffraction (SCXRD) data of undoped and La-doped Ca₂B₅O₉Cl that were obtained by flux method were collected at room temperature using a Rigaku XtaLab mini II diffractometer (Mo K α radiation). The data collection covered 99% of the reciprocal space to $2\theta_{\max} = 61.0^\circ$ with $R_{\text{int}} = 5.64\%$ (undoped phase) and 3.01% (La-doped phase) after absorption correction. The crystal structures were solved by a dual-space algorithm method (SHELXT)¹ and refined by a full-matrix least-squares method with SHELXL², using an Olex2 graphical user interface³.

Laboratory X-ray Powder Diffraction. Powder X-ray diffraction (PXRD) measurements of (Ca_{1-x}La_x)₂B₅O₉Cl_{1+2x} ($x = 0, 0.05, 0.10, 0.125, 0.15$) powder samples were performed using a Rigaku MiniFlex600 diffractometer (Cu K α radiation) in the 2θ range from 5° to 60° at room temperature.

Thermal Gravimetric Analysis. Thermogravimetric analysis (TGA) of $x = 0.10$ powder samples were performed using a Rigaku TG-DTA8188 system under flowing N₂ atmosphere (1.0 L/min). The sample was loaded in an alumina crucible and heated up to 700°C at 10°C/min.

Electrochemical impedance spectroscopy (EIS) measurements. (Ca_{1-x}La_x)₂B₅O₉Cl_{1+2x} ($x = 0, 0.05, 0.10$) powder samples were pelletized by pressing at 100 kN with diameter and thickness of 10 mm and 1 mm, respectively, followed by a second sintering with the same heating conditions. These obtained pellets were polished with waterproof abrasive papers until they were less than 0.6 mm thick. Formation of a gold sputtering layer in the center of the pellet surface using an ion coater (IB-3, Eiko), and then a gold paste was fixed on the sputtered layer. Ac EIS of the pellets was measured using the complex impedance method (1260 impedance per gain analyzer, Solartron) at 300 mV in the frequency range between 1 Hz and 10 MHz, starting at 400°C and testing at 100°C intervals up to 700°C in an Ar gas atmosphere. The Nyquist plot was fitted by using an equivalent circuit model composed of a total resistance (R_{total}), its constant phase element (CPE_{total}), an electrode-electrolyte interface resistance (R_i), and its constant phase element (CPE_i), as shown in Figures 4 and S5. The ac conductivity (σ_{ac}) was estimated from the total resistance. In order to investigate polarization behavior, dc conductivity (σ_{dc}) was calculated as a function of time at 700°C in an Ar gas atmosphere by applying a dc current of 0.1 μ A using a dc voltage/current generator (R6144, Advantest) and an electrometer (R8240, Advantest).

Computational Methods. The formation energies of point defects in Ca₂B₅O₉Cl were evaluated using first-principles total energy calculations. First, we optimized the unit cell and positional parameters of Ca₂B₅O₉Cl. To calculate point defects, a supercell model containing $1 \times 1 \times 2$ optimized unit cells was constructed. The total number of atoms in the perfect supercell model was 126. In this study, we investigated the following point defects: B vacancy (V_B), O vacancy (V_O), Cl vacancy (V_{Cl}), Ca vacancy (V_{Ca}), substitutional La at Ca site (La_{Ca}), interstitial O (O_i), and interstitial Cl (Cl_i). All the sites for each defect

type were calculated. Candidates for interstitial sites of O and Cl were generated based on Voronoi polyhedral using the pymatgen code⁴.

The formation energies of point defects, $E_f(D^q)$, are obtained using the following relation^[2], (1)

$$E_f(D^q) = \{E(D^q) + E_{\text{corr}}(D^q)\} - E(\text{perfect}) - \sum_i n_i \mu_i + q(\varepsilon_{\text{VBM}} + \Delta\varepsilon_F)$$

where $E(D^q)$ and $E(\text{perfect})$ are the total energies of a supercell with a defect D in the charge state q and of a perfect crystal supercell, respectively. n_i represents the number of i atoms removed ($n_i < 0$) or added ($n_i > 0$) to form defect D , and μ_i is the chemical potential of atom i . ε_{VBM} denotes the energy level of the valence band maximum, and $\Delta\varepsilon_f$ represents the Fermi level referenced to ε_{VBM} . $E_{\text{corr}}(D^q)$ corresponds to the sum of the image charge and potential alignment correction.⁵ To determine the chemical potentials, we considered the condition of oxidation and chloridation limits that are consistent with the experimental conditions. Chemical potentials for the elements other than O and Cl were determined from the most stable phase in equilibrium on the convex hull in free energy-composition plots. The convex hull was obtained by calculating all possible phases in the system recorded in the Materials Project⁶.

First-principles calculations based on DFT were performed to investigate the optimized structure, defect formation energy, and migration energy using the projector augmented-wave (PAW) method implemented in the VASP code⁷⁻¹⁰. The exchange-correlation term was treated with GGA-PBE¹¹. The plane-wave cutoff energy was set to 550 eV. Integration in reciprocal spaces for the $\text{Ca}_2\text{B}_5\text{O}_9\text{Cl}$ supercell was performed using $2 \times 2 \times 4$ and $2 \times 2 \times 2$ Γ -centered grids for the unit cell and supercell, respectively. Structure optimization was conducted until all residual forces acting on each atom were less than 0.01 eV/Å. First-principles molecular dynamics simulations were also performed for Cl_i - La_{Ca} association model and O_i model with the NVT ensemble. The simulation cells were the same as those used for the point defect. The total simulation time was 100 ps with an MD time step of 2 fs. The first 10 ps were removed from the analysis. The temperature was set to 2000 K to detect atomic jumps, though it is higher than the experimental conditions. The migration energies of Cl_i ion via the interstitialcy mechanism were calculated using the nudged elastic band (NEB) method^{12,13} with three intermediate images.

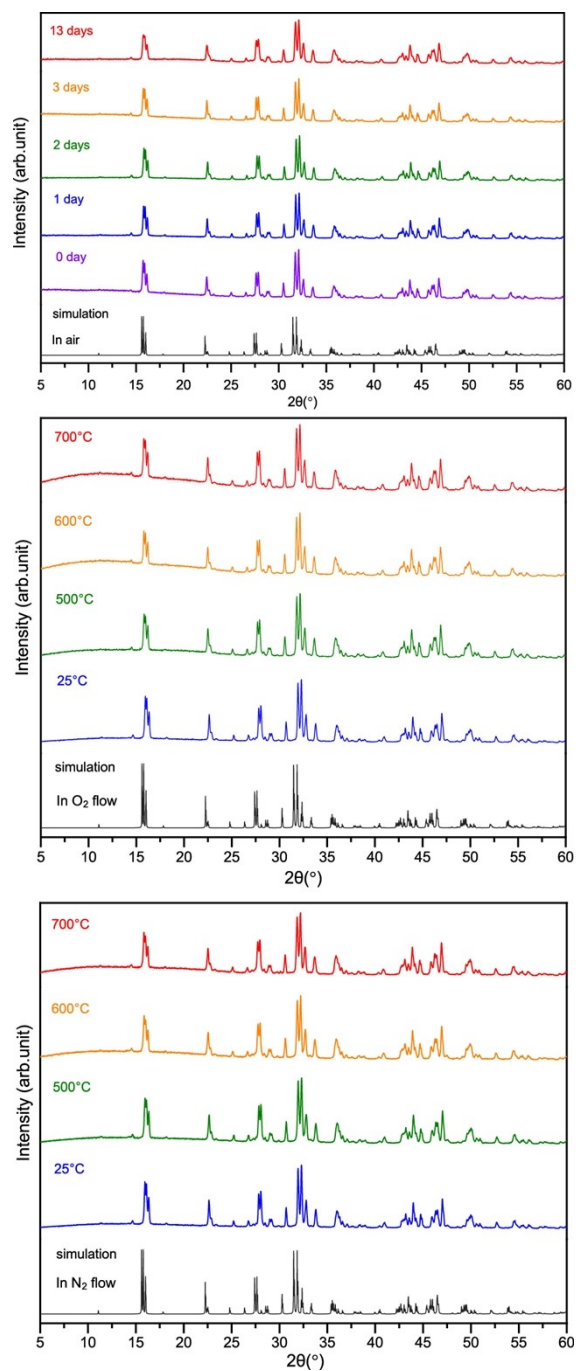


Figure S1. Stability of $\text{Ca}_2\text{B}_5\text{O}_9\text{Cl}$ in air, O_2 , and N_2 gas atmospheres. Room-temperature PXRD patterns collected from the borate chloride after 1–13 days of exposure to air and after heating at several temperatures in O_2 or N_2 gas atmosphere. No change in XRD patterns was observed under these experimental conditions.

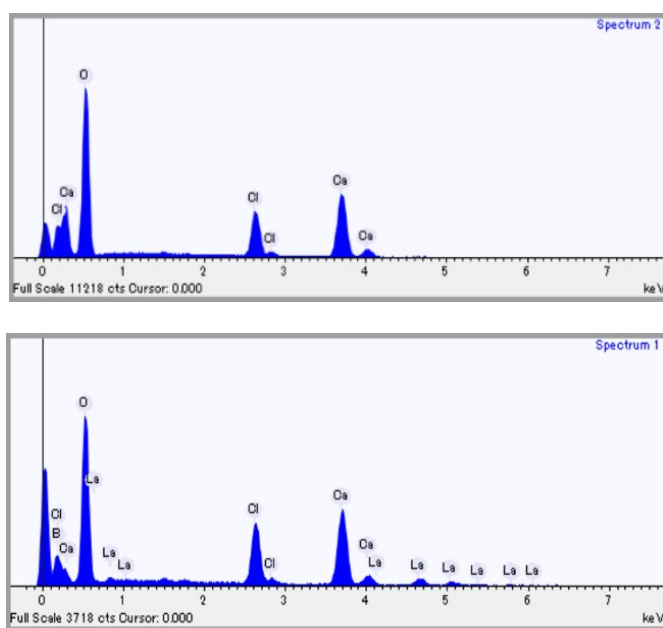


Figure S2. Photographs of single crystals of undoped(left) and La-doped(right) $\text{Ca}_2\text{B}_5\text{O}_9\text{Cl}$ on a 1mm-grid paper. The single crystals grew preferentially along the crystallographic c -axis.

Figure S3. EDX spectra of undoped (upper panel) and La-doped (lower panel) $\text{Ca}_2\text{B}_5\text{O}_9\text{Cl}$. The EDX analysis indicates that the molar ratio of Ca/Cl/La is 2.00/1.14/0 and 1.80/1.21/0.21, which are consistent with the results of single-crystal structure analysis.

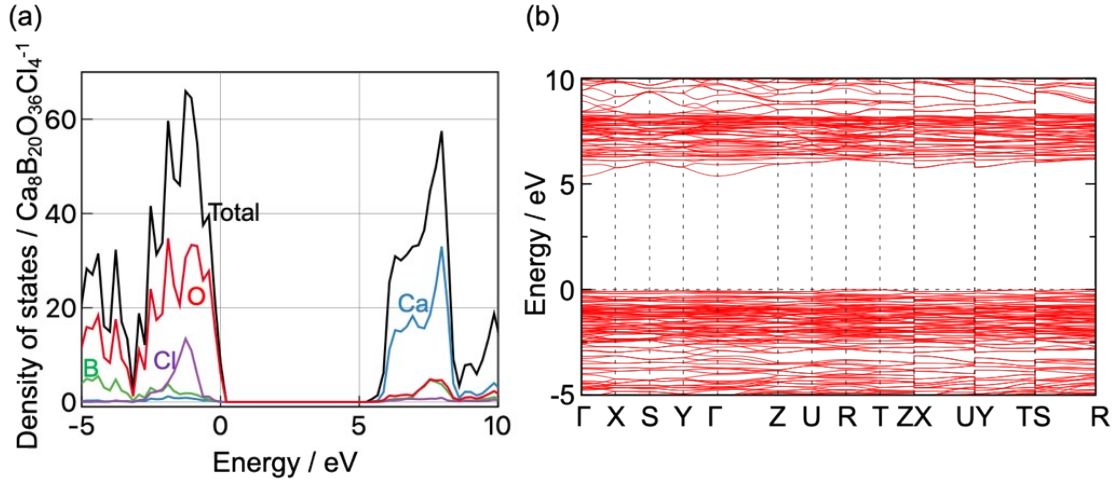


Figure S4. (a) Total and partial density of states and (b) band diagrams of $\text{Ca}_2\text{B}_2\text{O}_9\text{Cl}$. The band gap value was calculated to be 5.4 eV, very close to that previously reported value obtained by DFT calculations using the PBEsol exchange-correlation functional. The band gap value estimated from UV-vis spectrum is 7.3 eV.¹⁴ Underestimation of the band gap value is typical of DFT calculations using semi-local functionals.

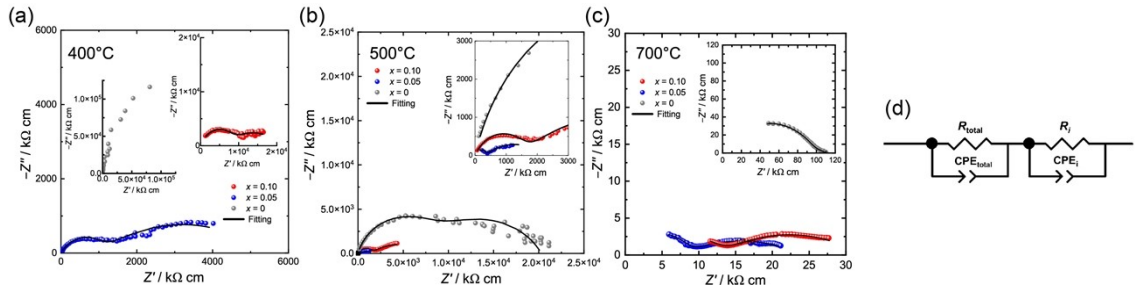


Figure S5. (a-c) Representative Nyquist plots of $(\text{Ca}_{1-x}\text{La}_x)_2\text{B}_2\text{O}_9\text{Cl}_{1+2x}$ ($x = 0, 0.05, 0.10$) recorded at 400, 500, and 700°C in an Ar gas atmosphere. (d) Equivalent circuit model used to fit all data: a total resistance (R_{total}) including bulk and grain-boundary resistances, its constant phase element ($\text{CPE}_{\text{total}}$), an electrode-electrolyte interface resistivity (R_i), and its constant phase elements (CPE_i). For the Nyquist plot of $x = 0$ at 400°C, since only a part of the semicircle was observed, it is difficult to fit the data using the equivalent circuit model.

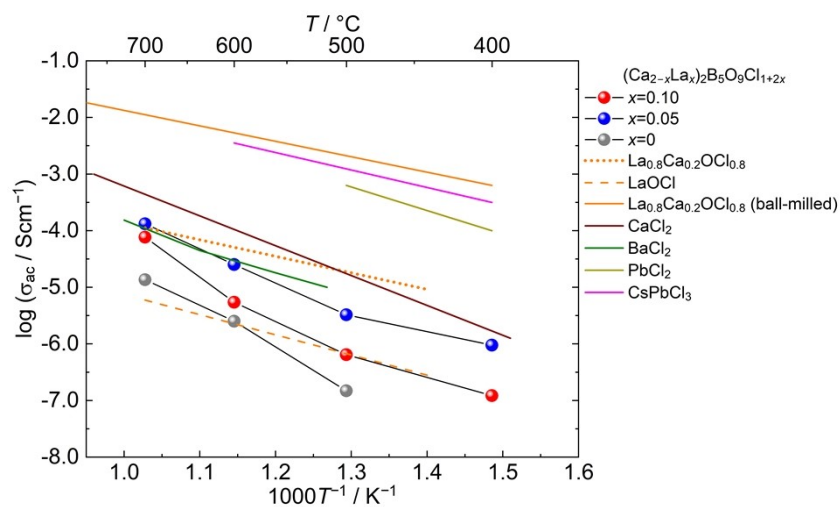


Figure S6. Comparison of the ac conductivity of $(\text{Ca}_{1-x}\text{La}_x)_2\text{B}_5\text{O}_9\text{Cl}_{1+2x}$ ($x = 0, 0.05, 0.10$) with those of conventional chloride-ion conductors¹⁵⁻¹⁸.

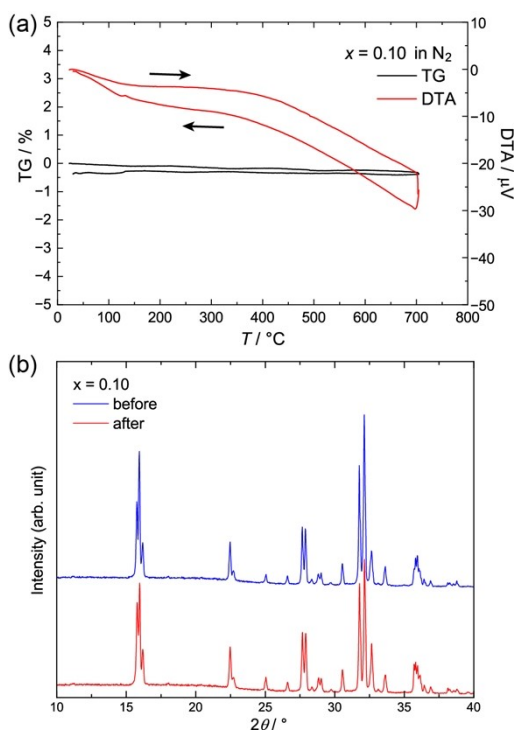


Figure S7. (a) TG-DTA curves of $x = 0.10$ in a N_2 gas atmosphere. The weight change was negligible within the instrumental resolutions. (b) Room-temperature PXRD patterns of $x = 0.10$ before and after the TG-DTA measurements. It remained unchanged after heating up to 700°C in N_2 gas.

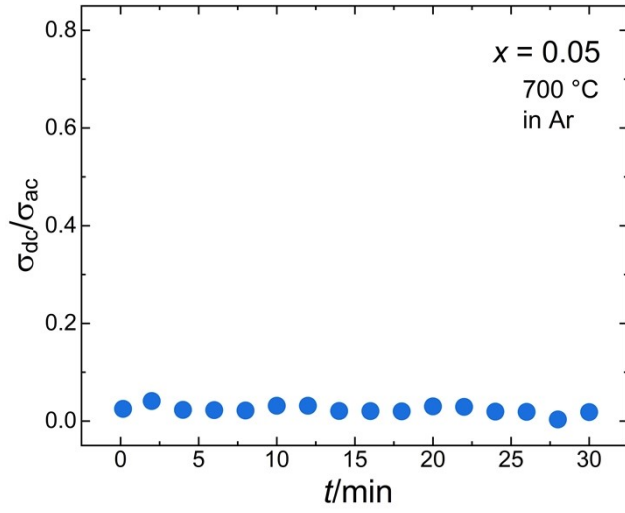
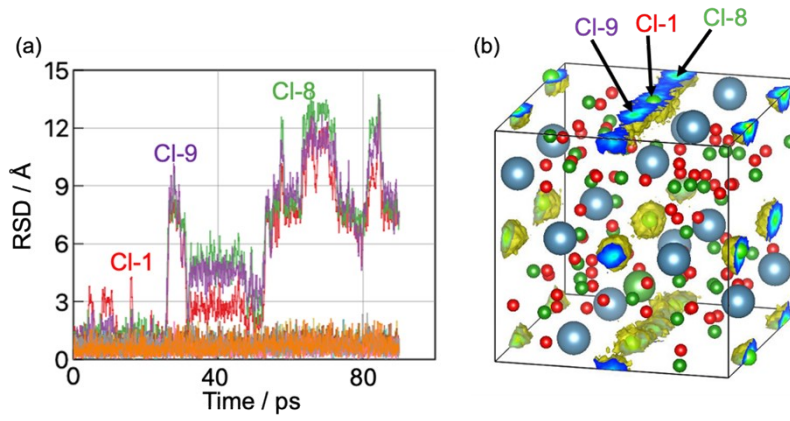


Figure S8. Polarization behavior for $(\text{Ca}_{1-x}\text{La}_x)_2\text{B}_5\text{O}_9\text{Cl}_{1+2x}$ ($x = 0.05$) in Ar gas atmosphere at 700°C .

Figure S9. (a) Root square displacements (RSD) for each Cl during MD simulations of the model containing a complex defect of La_{Ca}



and Cl_i. (b) Cl-1, Cl-8, and Cl-9 atoms in (a).

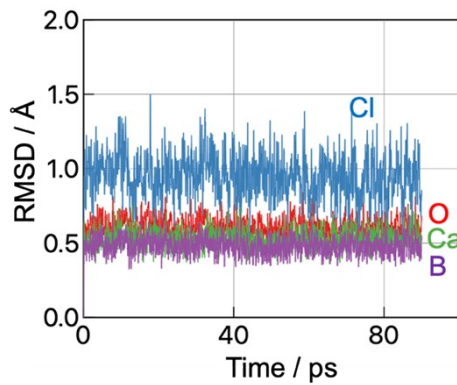


Figure S10. Root mean square displacements (RMSD) for the O_i model during MD simulations.

Table S1. Results of Structure Refinement of undoped and La-doped Ca₂B₅O₉Cl Using Single-Crystal XRD Data.

Formula	Ca ₂ B ₅ O ₉ Cl	(Ca _{0.92} La _{0.08}) ₂ B ₅ O ₉ Cl _{1.16}
Formula weight	313.66	335.14
Radiation	Mo K α ($\lambda=0.71073$ Å)	Mo K α ($\lambda=0.71073$ Å)
T (K)	293	293
Crystal system	Orthorhombic	Orthorhombic
Space group	<i>Pnn2</i>	<i>Pnn2</i>
a (Å)	11.3572(5)	11.3807(5)
b (Å)	11.2309(4)	11.3109(6)
c (Å)	6.3500(3)	6.3692(3)
V (Å ³)	809.95(6)	819.88(7)
Z	4	4
D _{calc} (g/cm ³)	2.572	2.703
F ₀₀₀	616	648
no. of measured reflns	11503	5926
no. of unique reflns	2391	1636
no. of observed reflns ($F^2 > 2\sigma(F^2)$)	2391	1636
R _{int} (%)	5.64	3.01
R[F ² > 2 σ (F ²)]/wR(F ²) (%)	4.34/6.53	2.87/5.87
GoF	1.07	1.08

Table S2. Refined Structural Parameters for the Single Crystal of Ca₂B₅O₉Cl.

atom	site	x	y	z	SOF ¹	$U_{iso}/\text{\AA}^2 \times 10^2$
Ca1	4c	-0.02906(8)	0.25646(8)	0.52456(15)	1	1.144(19)
Ca2	4c	-0.24359(9)	-0.03237(8)	0.35193(16)	1	1.030(19)
B1	4c	-0.1971(4)	0.2277(4)	0.0222(8)	1	0.65(9)
B2	4c	-0.3114(4)	0.2934(4)	0.3366(9)	1	0.67(9)
B3	4c	-0.2730(4)	0.1818(4)	0.6614(8)	1	0.56(10)
B4	4c	-0.2301(4)	0.0167(4)	0.8967(8)	1	0.80(11)
B5	4c	0.0237(4)	0.2576(4)	1.0655(7)	1	0.82(11)
O1	4c	-0.0905(3)	0.2672(2)	0.1319(4)	1	0.94(7)
O2	4c	-0.2959(2)	0.2978(3)	0.1084(5)	1	0.54(6)
O3	4c	-0.2753(3)	0.4006(2)	0.4579(5)	1	1.31(7)
O4	4c	-0.2479(3)	0.1950(2)	0.4391(4)	1	0.66(6)
O5	4c	-0.1903(2)	0.2534(2)	0.7928(5)	1	0.63(6)
O6	4c	-0.2559(2)	0.0516(3)	0.6977(5)	1	1.02(7)
O7	4c	-0.2139(3)	0.0972(2)	1.0570(4)	1	0.97(7)
O8	4c	0.0573(3)	0.2226(3)	0.8667(5)	1	1.08(7)
O9	4c	0.1040(3)	0.2856(3)	0.2185(5)	1	0.95(6)
Cl1	2a	0	0.5	0.6866(3)	1	2.00(4)
Cl2	2b	0	0	0.4261(3)	1	1.75(4)

¹ SOF stands for site occupancy factor.

Table S3. Anisotropic Displacement Parameters U_{ij} (\AA^2) for Ca₂B₅O₉Cl.

atom	U_{11}	U_{22}	U_{33}	U_{23}	U_{13}	U_{12}
Ca1	0.0134(4)	0.0133(4)	0.0075(4)	-0.0001(4)	0.0014(4)	-0.0022(4)
Ca2	0.0138(5)	0.0105(4)	0.0066(4)	0.0000(4)	-0.0014(5)	-0.0016(4)
B1	0.009(2)	0.005(2)	0.006(2)	-0.0022(19)	-0.002(2)	0.0002(16)
B2	0.005(3)	0.009(2)	0.006(2)	-0.002(2)	0.001(2)	-0.0015(18)

B3	0.004(2)	0.007(2)	0.006(2)	0.0003(17)	-0.0016(19)	-0.0029(17)
B4	0.007(2)	0.009(2)	0.007(3)	0.0002(18)	-0.0004(19)	0.0017(18)
B5	0.008(2)	0.007(2)	0.009(3)	0.0038(18)	0.003(2)	-0.002(2)
O1	0.0047(15)	0.0184(17)	0.0051(16)	-0.0032(13)	0.0004(12)	0.0000(12)
O2	0.0052(15)	0.0071(15)	0.0040(15)	0.0003(12)	-0.0012(12)	0.0020(11)
O3	0.027(2)	0.0050(15)	0.0070(16)	-0.0002(12)	-0.0026(14)	-0.0039(13)
O4	0.0086(16)	0.0066(15)	0.0045(14)	0.0003(12)	-0.0007(13)	0.0011(11)
O5	0.0048(16)	0.0098(15)	0.0043(14)	-0.0017(12)	0.0011(11)	-0.0002(12)
O6	0.0180(17)	0.0041(16)	0.0084(16)	0.0010(12)	-0.0018(16)	0.0006(12)
O7	0.0184(17)	0.0079(15)	0.0028(16)	-0.0008(12)	-0.0006(13)	0.0020(12)
O8	0.0069(15)	0.0180(16)	0.0074(16)	-0.0033(13)	0.0010(15)	-0.0014(12)
O9	0.0057(15)	0.0175(15)	0.0053(15)	-0.0020(12)	-0.0003(13)	-0.0013(12)
Cl1	0.0189(9)	0.0135(8)	0.0277(10)	0.000	0.000	-0.0013(6)
Cl2	0.0108(8)	0.0127(8)	0.0289(9)	0.000	0.000	-0.0010(6)

Table S4. Refined Structural Parameters for the Single Crystal of $(\text{Ca}_{0.92}\text{La}_{0.08})_2\text{B}_5\text{O}_9\text{Cl}_{1.16}$.

atom	site	x	y	z	SOF ¹	$U_{\text{iso}}/\text{\AA}^2 \times 10^2$
Ca1	4c	-0.02098	0.26466	0.52476	0.889	1.95(3)
Ca2	4c	-0.24941	-0.02796	0.35481	0.957	1.46(3)
La1	4c	-0.02098	0.26466	0.52476	0.111	1.95(3)
La2	4c	-0.24941	-0.02796	0.35481	0.043	1.46(3)
B1	4c	-0.1904	0.2292	0.0255	1	0.94(11)
B2	4c	-0.3021(5)	0.3006(5)	0.3374(10)	1	0.96(11)
B3	4c	-0.2641(5)	0.1907(5)	0.6640(9)	1	0.90(12)
B4	4c	-0.2329(5)	0.0237(5)	0.8980(10)	1	1.23(15)
B5	4c	0.0332(5)	0.2494(5)	1.0637(10)	1	1.23(15)

O1	4c	-0.0799(3)	0.2559(3)	0.1342(6)	1	1.74(9)
O2	4c	-0.2699(3)	0.4083(3)	0.4597(6)	1	1.88(9)
O3	4c	-0.2824(3)	0.3072(3)	0.1134(6)	1	1.12(8)
O4	4c	-0.2372(3)	0.2041(3)	0.4431(6)	1	1.16(8)
O5	4c	-0.1803(3)	0.2561(3)	0.7967(6)	1	0.96(8)
O6	4c	-0.2508(3)	0.0602(3)	0.6969(6)	1	1.44(8)
O7	4c	-0.2204(3)	0.1028(3)	1.0592(6)	1	1.52(8)
O8	4c	0.0674(3)	0.2192(3)	0.8646(6)	1	1.39(8)
O9	4c	0.1147(3)	0.2718(3)	0.2198(6)	1	1.32(8)
Cl1A	2b	0	0.5	0.6876	0.65	2.99(8)
Cl1B	2b	0	0.5	0.515	0.102	2.99(11)
Cl1C	2b	0	0.5	0.354	0.216	2.99(11)
Cl1D	2b	0	0.5	0.861	0.214	2.99(11)
Cl1E	2b	0	0.5	1.018	0.123	2.99(11)
Cl2	2a	0	0	0.4277	0.954	1.77(6)

¹ SOF stands for site occupancy factor.

Table S5. Anisotropic Displacement Parameters U_{ij} (\AA^2) for $(\text{Ca}_{0.92}\text{La}_{0.08})_2\text{B}_5\text{O}_9\text{Cl}_{1.16}$.

atom	U_{11}	U_{22}	U_{33}	U_{23}	U_{13}	U_{12}
Ca1	0.0129(4)	0.0382(6)	0.0073(4)	0.0016(5)	0.0011(4)	0.0011(4)
Ca2	0.0247(5)	0.0116(5)	0.0075(5)	0.0012(4)	0.0001(4)	-0.0040(4)
La1	0.0129(4)	0.0382(6)	0.0073(4)	0.0016(5)	0.0011(4)	0.0011(4)
La2	0.0247(5)	0.0116(5)	0.0075(5)	0.0012(4)	0.0001(4)	-0.0040(4)
B1	0.008(2)	0.009(2)	0.011(3)	0.002(3)	-0.004(3)	-0.002(2)
B2	0.007(2)	0.012(3)	0.009(3)	0.000(2)	0.000(2)	0.002(2)
B3	0.005(3)	0.009(3)	0.013(3)	0.003(2)	0.000(2)	0.002(2)
B4	0.014(3)	0.012(3)	0.011(5)	0.000(2)	0.001(2)	0.000(2)

B5	0.010(2)	0.012(3)	0.015(5)	0.000(2)	-0.004(3)	0.000(3)
O1	0.0071(16)	0.033(2)	0.012(2)	-0.0025(17)	-0.0004(15)	-0.0032(16)
O2	0.034(2)	0.0117(17)	0.0106(19)	-0.0005(15)	-0.0012(17)	-0.0058(17)
O3	0.0167(18)	0.0129(18)	0.0040(18)	0.0010(15)	-0.0008(15)	0.0052(14)
O4	0.0137(17)	0.0148(17)	0.0062(17)	0.0009(14)	0.0022(15)	0.0050(15)
O5	0.0115(18)	0.0105(17)	0.0068(18)	0.0005(13)	0.0004(14)	-0.0008(15)
O6	0.025(2)	0.0094(19)	0.009(2)	-0.0008(16)	-0.0020(17)	0.0012(15)
O7	0.0271(19)	0.0094(17)	0.009(2)	-0.0020(15)	0.0008(16)	-0.0018(15)
O8	0.0076(17)	0.0242(19)	0.010(2)	-0.0042(16)	0.0009(17)	-0.0007(14)
O9	0.0082(17)	0.0238(19)	0.0077(18)	-0.0007(16)	-0.0015(15)	-0.0023(15)
C11A	0.0269(15)	0.0145(16)	0.0485(17)	0.000	0.000	-0.0002(13)
C11B	0.027(2)	0.0145(15)	0.0485(16)	0.000	0.000	-0.0002(17)
C11C	0.027(2)	0.0145(15)	0.0485(16)	0.000	0.000	-0.0002(17)
C11D	0.027(2)	0.0145(15)	0.0485(16)	0.000	0.000	-0.0002(17)
C11E	0.027(2)	0.0145(15)	0.0485(16)	0.000	0.000	-0.0002(17)
C12	0.0088(9)	0.0147(10)	0.0296(12)	0.000	0.000	-0.0005(7)

References

- 1 G. M. Sheldrick, *Acta Crystallogr A*, 2015, **71**, 3–8.
- 2 C. B. Hubschle, G. M. Sheldrick and B. Dittrich, *J Appl Crystallogr*, 2011, **44**, 1281–1284.
- 3 O. V. Dolomanov, A. J. Blake, N. R. Champness and M. Schröder, *J Appl Crystallogr*, 2003, **36**, 1283–1284.
- 4 S. P. Ong, W. D. Richards, A. Jain, G. Hautier, M. Kocher, S. Cholia, D. Gunter, V. L. Chevrier, K. A. Persson and G. Ceder, *Comput Mater Sci*, 2013, **68**, 314–319.
- 5 Y. Kumagai and F. Oba, *Phys Rev B*, 2014, **89**, 195205.
- 6 A. Jain, S. P. Ong, G. Hautier, W. Chen, W. D. Richards, S. Dacek, S. Cholia, D. Gunter, D. Skinner, G. Ceder and K. A. Persson, *APL Mater*, 2013, **1**, 011002.
- 7 G. Kresse and D. Joubert, *Phys Rev B*, 1999, **59**, 1758–1775.
- 8 G. Kresse and J. Furthmüller, *Phys Rev B*, 1996, **54**, 11169–11186.
- 9 G. Kresse and J. Furthmüller, *Comput Mater Sci*, 1996, **6**, 15–50.
- 10 G. Kresse and J. Hafner, *Phys Rev B Condens Matter*, 1993, **47**, 558–561.
- 11 J. P. Perdew, A. Ruzsinszky, G. I. Csonka, O. A. Vydrov, G. E. Scuseria, L. A. Constantin, X. Zhou and K. Burke, *Phys Rev Lett*, 2008, **100**, 136406.
- 12 G. Henkelman and H. Jónsson, *J Chem Phys*, 2000, **113**, 9978–9985.
- 13 G. Henkelman, B. P. Uberuaga and H. Jónsson, *J Chem Phys*, 2000, **113**, 9901–9904.
- 14 Z. Wang, J. He, B. Hu, P. Shan, Z. Xiong, R. Su, C. He, X. Yang and X. Long, *ACS Appl Mater Interfaces*, 2020, **12**, 4632–4637.
- 15 N. Nunotani, M. R. I. Bin Misran, M. Inada, T. Uchiyama, Y. Uchimoto and N. Imanaka, *Journal of the American Ceramic Society*, 2020, **103**, 297–303.
- 16 N. Imanaka, K. Okamoto and G. Y. Adachi, *Angewandte Chemie - International Edition*, 2002, **41**, 3890–3892.
- 17 C. E. Derrington, A. Lindner and M. O'keeffe, *Ionic Conductivity of Some Alkaline Earth Halides*, 1975, vol. 15.
- 18 J. Mizusaki, K. Arai and K. Fueki, *IONIC CONDUCTION OF THE PEROVSKITE-TYPE HALIDES*, North-Holland Publishing Company, 1983, vol. 11.